INSTITUTE OF PHYSICS PUBLISHING JOURNAL OF GEOPHYSICS AND ENGINEERING
J. Geophys. Eng. **3** (2006) 194–205 doi:10.1088/1742-2132/3/2/010

Limitations in qualitative and quantitative analysis of time-lapse data due to fluid flow uncertainties

Jason K Furtney and Andrew W Woods

BP Institute, Cambridge University, Madingly Road, Cambridge CB3 0EZ, UK

Received 6 July 2005
Accepted for publication 21 March 2006
Published 11 May 2006
Online at stacks.iop.org/JGE/3/194

Abstract
We address some limitations in qualitative and quantitative analysis of time-lapse data due to underlying uncertainties in the flow of reservoir fluids. We explore how seismic signals may evolve over time by developing synthetic time-lapse data based on a variety of flow scenarios including radial flow, multi-phase flow and flows with unstable mobility ratios. Model predictions of water saturation and effective stress are used to construct synthetic impedance profiles. Using an idealized model of water-flood type production we show that qualitative analysis can be limited by the signal complexities resulting from flows in which both water saturation and effective stress change gradually, such as may occur when the injected water and the displaced oil are not separated by a sharp interface. A two-layer reservoir flow model is developed with which the limitations of quantitative analysis are explored. If a quantitative inversion technique is error free the resolution limits and signal noise in the seismic data allow only spatially averaged reservoir properties to be known. In some reservoirs undergoing water flood, volumetrically significant movement of the injected water may occur on length scales below that of the resolution and noise threshold the seismic data allows. In such a reservoir the inversion technique gives good quality information about the average location of the injected water but does not provide information about how all the injected water is moving. Specifically the possibility of thin high permeability layering carrying a significant fraction of the injected water cannot be eliminated. We show that this can introduce great uncertainty in estimates of reservoir performance.

Keywords: time-lapse seismic, reservoir monitoring, reservoir simulation, multi-phase flow

1. Introduction

Time-lapse seismic surveys are becoming a fully integrated component of the field management process in many oil companies (Calvert 2005, Raikes *et al* 2003, Gawith *et al* 1996). In many cases time-lapse seismic has been successful as a qualitative tool for identifying zones where the pressure and saturation have evolved in comparison to quiet zones. This type of information has been used in determining the best sites to locate new wells (Gawith *et al* 1996, Parr and Marsh 2000, Stronen *et al* 2003). This type of analysis is most effective when one production-related effect dominates the change in amplitude. When two or more production effects have equal influence on the amplitude change this type of analysis becomes challenging. However, quantitative analysis, such as deriving estimates of the spatial distribution of water saturation and effective stress from time-lapse data, is beginning to become a reality (Stovas and Landro 2005, Behrens *et al* 2004, Duffaut *et al* 2003, Landro 2001, Brevik 1999). This type of information is used in forward modelling of reservoir performance.

This paper explores some of the limitations associated with deriving qualitative and quantitative information from time-lapse data by developing synthetic time-lapse data based on simple flow principles and a basic model of rock properties. Landro (2002) gives a formal mathematical uncertainty analysis of time-lapse seismic analysis based on the uncertainty of each parameter in the inversion (Landro

2002). Our approach differs in that we use flow models as a source of uncertainty and analyse the resulting idealized synthetic time-lapse data. Using a water-flood-type flow we contrast the influence of fluid saturation and pore pressure on the time-lapse seismic signal in a variety of flow scenarios. This model is used to illustrate limitations on the qualitative interpretation of time-lapse seismic data which may arise as the result of fluid instabilities and mixing. A two-layer reservoir model is developed to illustrate some limitations on quantitative analysis of time-lapse seismic data.

2. Rock physics

Recently much work has been carried out to invert time-lapse data back to original physical parameters using advanced seismic data collection and processing and sophisticated rock physics models. In the present work some of the fundamental underlying uncertainties in data interpretation, due to the nature of the fluid movement in the reservoir, are illustrated and for this purpose a greatly simplified rock physics model is developed in this section.

It is assumed that the vertical extent of the reservoir horizon of interest is around 25 m, the possible limit of the resolution of the seismic waves. Because changes are occurring only in this zone, the reservoir will be represented as a single reflection horizon in seismic data; further, only a single normal incidence reflection is considered. For a wave of normal incidence, the amount of energy reflected back to the surface at a given interface is related to the acoustic impedance of the rocks on either side of the interface by the relation

$$\frac{a_r}{a_i} = \frac{I_2 - I_1}{I_2 + I_1} \tag{2.1}$$

where I_1 and I_2 are the acoustic impedances of the upper and lower layers, and a_i and a_r are the amplitudes of the incident and reflected waves. This is the one-dimensional normal-incidence case of the Zoeppritz equations (Sherriff and Geldart 1995). The acoustic impedance I of a rock is

$$I = \rho V_p, \tag{2.2}$$

where ρ is the density, and V_p is the compressional wave velocity of the rock. The compressional wave velocity is given by

$$V_p = \sqrt{\frac{\bar{\kappa}}{\rho}} \tag{2.3}$$

where $\bar{\kappa}$ is the compressional wave modulus of the rock, which describes the elastic behaviour of the material under compressive stresses. The equations can be combined to give impedance directly with units (kg m^{-3})(m s^{-1}):

$$I = \sqrt{\rho \bar{\kappa}}. \tag{2.4}$$

For the time-lapse method to be useful a method is needed to predict and interpret the changes in the impedance of a reservoir rock as production takes place. This paper focuses on water-flood-type production where a water injection well is used to sweep oil to a production well. During such production both the pressure and the saturation in the rock evolve. Typically, changes in the compressional wave modulus of rocks associated with these changes are one to two orders of magnitude greater than the accompanying change in density. Thus, for convenience, in estimating the acoustic impedance (2.4), it is assumed that the density remains constant. To calculate the impedance of the changing reservoir the compressional wave modulus of the rock needs to be calculated as the pore pressure and pore fluids change.

2.1. Stress relations

To calculate the impedance of a reservoir undergoing production, a model describing how the compressional wave modulus of a rock changes as the pore pressure changes is required. In a porous rock the weight of the overlying rock is supported by a combination of the rock matrix and the pore fluids. As the pore pressure decreases the porosity also decreases as more of the confining stress is supported by the rock frame. In rocks with pore fluids the rock 'feels' the confining stress minus the pore pressure. This is the effective stress, σ (Terzaghi 1943).

The compressional wave modulus given in (2.3) and (2.4) is a single parameter describing how the fluid-saturated rock deforms as long-wavelength compressional waves propagate downwards through it. However, experiments and field evidence have shown that as the effective stress in a reservoir changes due to production activities, the compressional wave modulus changes (Christensen and Wang 1985).

In practice rock core laboratory data are fitted to polynomial or logarithmic curves and scaled up to the reservoir size to estimate how the compressional wave modulus changes as a function of effective stress (Holt *et al* 2000). In order to create a simple representative model and maintain the key principles in the present work we model the compressional wave modulus change as a function of effective stress using relevant core data. A straight line is fitted within the region of effective stresses encountered in the model reservoir. Figure 1 shows laboratory core data showing an increasing compressional wave modulus with increasing effective stress in an oil-saturated reservoir rock. Because the slope of the compressional wave modulus is greater at lower pressures, a time-lapse signal resulting from changes in pressure will be more apparent in a lower pressure reservoir. The shaded zone in figure 1 is the range of effective stresses expected in the Magnus North Sea oil reservoir (Jack 1998, Gawith *et al* 1996). To describe how the compressional wave modulus changes in the present modelling a linear trend is fitted to these data within the shaded zone,

$$\bar{\kappa}(\sigma) = 466.0\sigma + 19.3 \times 10^9 \text{ (Pa)}, \tag{2.5}$$

for 10 MPa $< \sigma <$ 25 MPa.

2.2. Pore fluid change

Equation (2.5) describes how the compressional wave modulus changes due to an imposed pore pressure. However the presence of pore fluids also has an effect on the modulus of the rock. Changes in impedance in time-lapse data due to fluid substitution will be most apparent in high porosity reservoirs. The Gassmann relation is used in this work, as it assumes a

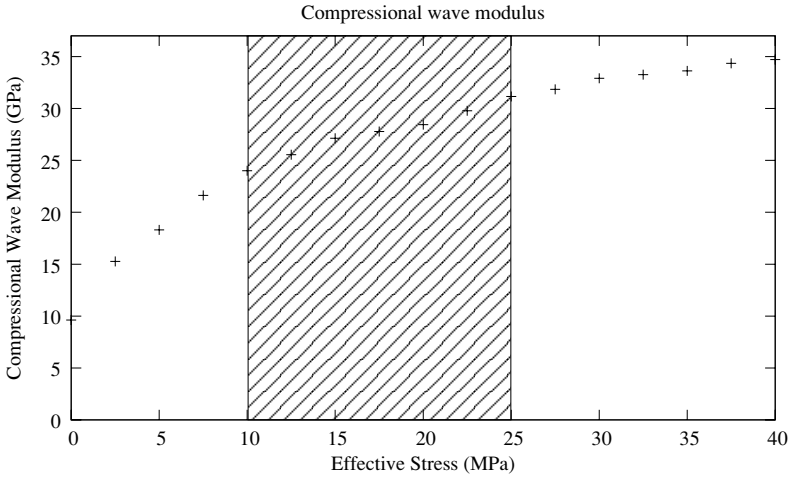

Figure 1. Laboratory data showing compressional wave modulus as a function of effective stress (Jack 1998, Gawith *et al* 1996).

low frequency wave typical of seismic exploration at reservoir depths,

$$\bar{\kappa} = \left(\kappa_{\text{dry}} + \kappa_{\text{gr}} \frac{\left(1 - \frac{\kappa_{\text{dry}}}{\kappa_{\text{gr}}}\right)^2}{1 - \frac{\kappa_{\text{dry}}}{\kappa_{\text{gr}}} - \phi + \frac{\phi \kappa_{\text{gr}}}{\kappa_{\text{fluid}}}} \right), \tag{2.6}$$

where $\bar{\kappa}$, κ_{dry} and κ_{gr} are the compressional wave moduli of the fluid-saturated rock, the dry frame and the grains respectively, ϕ is the porosity, ρ is the average density and κ_{fluid} is the bulk modulus of the pore fluids (Gassmann 1951). In the rock model calculations the value of $\bar{\kappa}$ is approximated from (2.5) and substituted into the κ_{dry} term of (2.6).

As a pore pressure gradient is imposed on the reservoir body by the wells, a small change in porosity is expected. Further, a porosity change is implicit in (2.5) as it is derived from physical data. However, for the purposes of the fluid substitution, (2.6), porosity is assumed to be constant because it has only a small influence on the bulk modulus during fluid substitution. In (2.6), a change in porosity of 5% results in a 0.5% change in $\bar{k}$ while the corresponding change in κ_{dry} (15 MPa, figure 1) results in a 33% change in $\bar{k}$.

Using the variable S to describe the water saturation, and assuming that the bulk modulus of the fluid mixture is a linear volume average of the individual end members' moduli, (2.5) is extended to include the effects of fluid substitution. Applying the Gassmann relation, with $\phi = 0.1$, $\kappa_{\text{water}} = 2.2$ GPa, $\kappa_{\text{oil}} = 150$ MPa, $\kappa_{\text{gr}} = 49$ GPa and $\kappa_{\text{dry}} = 24$ GPa, to a change in pore fluid from pure oil, $S = 0$, to pure water, $S = 1$, gives an increase in bulk modulus of 4.35 GPa. Combining this with the dependence on saturation (2.5) gives the general expression,

$$\bar{\kappa}(\sigma, S) = 466.0\sigma + 4.35 \times 10^9 S + 19.3 \times 10^9 \text{ (Pa)}, \tag{2.7}$$

for 10 MPa $< \sigma <$ 25 MPa and $0 > S > 1$.

A small density change is also expected due to the imposed pore pressure and is implicit in (2.5). For the purpose of calculating the synthetic impedance the density is taken as a constant because density changes have only a small influence on the impedance. A density change of 3%, as would be expected from a change in porosity of 5%, results in a 1.5% change in impedance compared to a 13% change in impedance due to a change in $\bar{k}$.

Using a constant density of 2600 kg m^{-3} with (2.4) yields a formula for impedance in terms of effective stress and water saturation. The resulting formula is nonlinear. However, for the range of values used herein, the data may be approximated by a linear function,

$$I(\sigma, S) = 6.67 \times 10^{-2}\sigma + 7.14 \times 10^5 S + 7.23 \times 10^6 \text{ (kg m}^{-3})(\text{m s}^{-1}) \tag{2.8}$$

for 10 MPa $< \sigma <$ 25 MPa and $0 > S > 1$. This model of impedance, representative of the Magnus field in the North Sea, is used as an example for the impedance calculations in this work. The impedance formula (2.8) shows that a typical fluid substitution, where 60–70% of the pore fluids are replaced, generates a change in impedance of about 6% and the change in impedance due to imposed pore pressure is about 10%.

3. Reservoir modelling

In order to establish the important principles of acoustic impedance change during water-flood-type production, a series of simplified one-dimensional models for a variety of reservoir flow scenarios are developed in this section. For the present modelling, the key predictions are the temporal and spatial evolution of effective stress, σ, and the water saturation, S, during water flooding.

The flow of oil and water in the reservoir is assumed to be governed by Darcy's law. When water-flood-type production begins in an oil reservoir, there is a transient period during which pressure disturbances, created by pumping at the wells, propagate through the reservoir. This transient period is controlled by the compressibility of the fluid and rock. It can be shown that this transient pressure period typically lasts from hours to days, while the movement of the fluid front and the interval of the time-lapse seismic measurements is

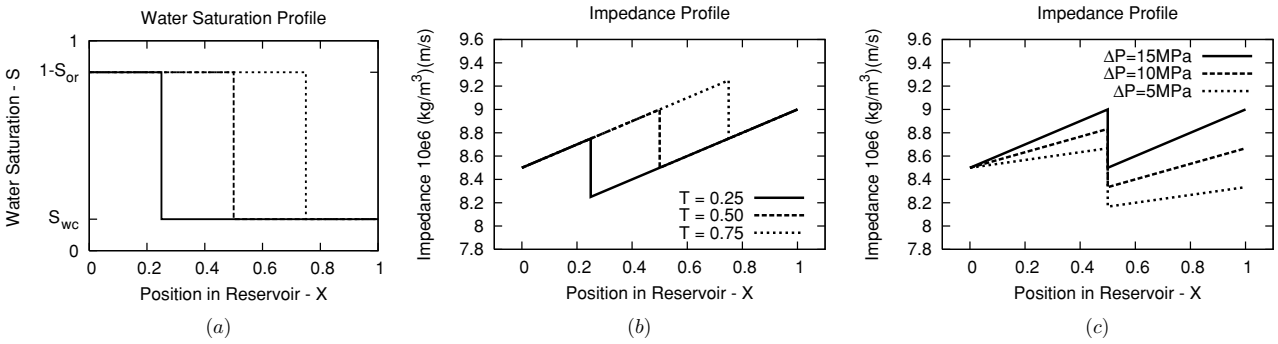

Figure 2. (*a*) Water saturation profile for $M = 1$. (*b*) Impedance profile for $M = 1$. (*c*) Impedance profiles for different values of ΔP.

on the scale of months to years (Dake 1994). Thus time-lapse seismic data are expected to record the migration of fluid fronts and the associated changes in the pressure, rather than the initial pressurization of the system associated with the onset of injection and production. In the present modelling, it is therefore assumed that a quasi-steady pressure distribution is reached throughout the model reservoir.

In order to establish some principles and gain insight into the temporal and spatial evolution of the acoustic impedance, the predictions of a hierarchy of models of increasing complexity are explored. In the first idealized model (section 3.1) the displacement of oil by injected water is modelled in a one-dimensional geometry and it is assumed that a sharp interface separates the mobilized oil and water. We also assume the oil and water have the same mobility. Section 3.2 explores the role of viscosity differences between the fluids, and the effects of fractional flow are explored in section 3.3. The analogous radial flow problem is investigated in section 3.5 and appendix A, and finally the effects of mixing between water and oil, due to frontal instabilities or capillary pressure, are explored in section 3.6. These models are far simpler than an actual oil reservoir, but they share many important features which allows us to gain insight into the controls on the time-lapse seismic signals expected in real reservoirs.

3.1. Simple Darcy flow model

Using Darcy's law, the Darcy velocity U is given by

$$U = -\frac{m_o}{\phi}\frac{dP}{dx}\bigg|_o - \frac{m_w}{\phi}\frac{dP}{dx}\bigg|_w \tag{3.1}$$

$$m_o = \frac{K_{oe}}{\mu_o}, \qquad m_w = \frac{K_{ow}}{\mu_w}, \tag{3.2}$$

$$M = \frac{m_w}{m_o} \tag{3.3}$$

where m is mobility, μ_w and μ_o are the dynamic viscosities of oil and water, ϕ is the porosity, and P is the pore pressure. K_{eo} is the effective permeability for oil flow if there is a small fraction of the pore space occupied by connate water and K_{ew} is the effective permeability for water flow if there is a small fraction of the pore space occupied by residual oil. The one-dimensional flow between a water injection well and a production well a distance L apart is considered. The injected water front is traced as it displaces the oil originally in place. The displacement is assumed to be incompressible and the pore pressure at the injection and production wells is kept constant. Further, it is assumed that $M = 1$ and a sharp interface separates the injected water and oil so that ahead of the interface, only oil moves, while behind the interface only water moves.

Because the fluids have the same mobility, the pressure gradient that drives the flow is constant in time and space. The wells impose a constant pressure increase and draw down so (3.1) becomes

$$U = -\frac{m_w}{\phi}\frac{P_{in} - P_{pr}}{L}, \tag{3.4}$$

where P_{in} and P_{pr} are the pore pressures at the injector well and producer well and L is the distance between the wells. To simplify the presentation, dimensionless position and time are used

$$X = \frac{x}{L} \qquad \text{and} \qquad T = \frac{tU}{L}. \tag{3.5}$$

With these dimensionless variables, water saturation can be written as

$$S(X,T) = \begin{cases} S_{wc} = 0.15 & X > T \\ 1 - S_{or} = 0.85 & X < T. \end{cases} \tag{3.6}$$

Figure 2(*a*) shows a time series of saturation profiles along the length of the reservoir. A sharp interface is seen propagating at a constant rate along the length of the reservoir. In this model, we assume that immobile residual oil remains behind the interface and immobile connate water is ahead of the interface.

3.1.1. Impedance calculation. The model distributions of saturation and effective stress are used to calculate the evolution of impedance, in this section. Now we use the flow model to calculate the evolution of impedance with time. In this case the pressure gradient driving the flow is linear and constant in time so the pore pressure can be written in terms of the dimensionless position X as

$$P = P_{in} - (P_{in} - P_{pr})X. \tag{3.7}$$

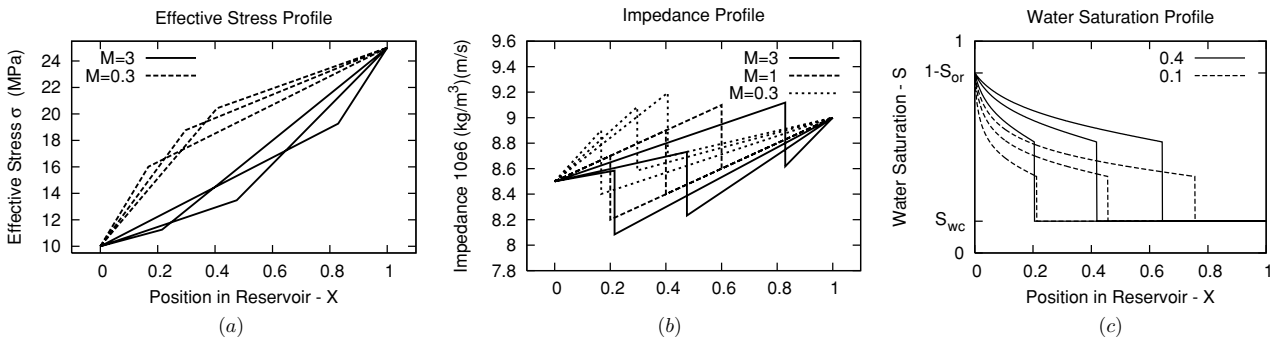

Figure 3. (*a*) Effective stress profiles for $M = 3$ and $M = 0.3$. (*b*) Impedance profiles for $M = 3$ and $M = 0.3$. (*c*) Water saturation profiles for a fractional flow.

The rock feels the effective stress, σ, which is the confining stress, σ_c, minus the pore pressure,

$$\sigma = \sigma_c - P. \tag{3.8}$$

We choose the confining stress to be 35 MPa and the injector pore pressure to be 25 MPa so the stress range corresponds to the linear range in figure 1. From (2.8) the impedance can be written as:

$$I = 6.67 \times 10^{-2} \Delta P X + 7.14 \times 10^{5} S + 7.89 \times 10^{6}\ (\text{km m}^{-3})(\text{m s}^{-1}) \tag{3.9}$$

$$\Delta P = P_{\text{in}} - P_{\text{pr}} \tag{3.10}$$

for $0 < x < 1$ and $0.85 > S > 0.15$.

Figure 2(*b*) shows a time series of impedance profiles of this simple displacement flow when $\Delta P = 15$ MPa. The impedance increases towards the production well as the effective stress increases, and a jump is seen in the signal at the fluid interface. Although this model is greatly simplified, it can be used to identify spatial and temporal characteristics of the change in impedance present in more complex models. If the pore pressure difference, ΔP, imposed by the wells is decreased, the rate of change of impedance with position will decrease. Figure 2(*c*) shows the impedance profile for a series of values of ΔP. As the size of the pore pressure difference between the wells decreases the rate of change of impedance with position decreases, but the size of the jump at the fluid interface remains the same.

3.2. *Contrasting mobility model*

In section 3.1 it was assumed that the mobility of the oil and water are the same, $M = 1$, which leads to a constant pressure gradient in space and time. However, oil and water often have different mobilities leading to different pressure gradients in front of and behind the water–oil interface. The current model is extended in this section to allow the fluid mobilities to differ, $M \neq 1$. For simplicity it is assumed that a sharp interface separates the mobilized oil and water, and the applied pressure difference between the wells is a constant. As a result of these assumptions a simple approach can be used to determine the pore pressure profile. In practice, when $M > 1$, frontal instabilities may develop as the water flood advances. We discuss the effects of this in section 3.6.

The mobility on either side of the interface is constant so the pore pressure can be written as,

$$P(X,T) = \begin{cases} \dfrac{X(1-P_{\text{wf}})}{X_{\text{wf}}} & X < X_{\text{wf}} \\ P_{\text{wf}} & X = X_{\text{wf}} \\ \dfrac{(X - X_{\text{wf}})P_{\text{wf}}}{1 - X_{\text{wf}}} & X > X_{\text{wf}}. \end{cases} \tag{3.11}$$

Calculating the impedance profiles of these flows requires the effective stress, which is given by (3.8). Effective stress profiles for flows with $M = 3$ and $M = 0.3$ are shown in figure 3(*a*) at three equally divided time steps. In section 3.1 where $M = 1$, the effective stress distribution is a straight line; when $M \neq 1$ the water and oil have different mobilities, forcing a different pressure gradient in each zone. When $M > 1$ ($M < 1$), the effective stress gradient in the oil zone is steeper (less steep) than the water zone at any instant because the oil is less mobile. The pressure gradients in both zones change as the flow progresses.

The rate at which the water front moves through the reservoir is not constant since mobile water is displacing less mobile oil. The following expression can be derived for the interface position, X_{wf}, as a function of time:

$$X_{\text{wf}}(T) = \frac{M - \sqrt{M^2 + 2MT - 2M^2 T}}{M - 1}. \tag{3.12}$$

For $M = 3$, corresponding to a viscous oil, the rate at which the interface moves through the reservoir increases with time as the less mobile oil is removed from the reservoir. For $M = 0.3$, corresponding to a low viscosity oil, the rate at which the front propagates decreases.

The effective stress distribution given by (3.11) and (3.8) can be combined with (2.8) to give the model impedance at any point. Figure 3(*b*) shows impedance profiles of a flow with $M = 3$ in solid lines, $M = 0.3$ in dotted lines and the $M = 1$ flow, from section 3.1, in dashed lines. The time interval between each profile is the same for all three flows. The general upward trend in impedance is the same in all three flows, as a result of the increasing effective stress. The $M = 3$ flow progresses further than the $M = 1$ flow each time step because the Darcy velocity increases as the less mobile oil is removed from the system. The $M = 0.3$ flow moves through the reservoir at a lower rate then the $M = 1$ flow because a

relatively low mobility water is replacing the oil. The rate of change of impedance with position is constant for all times when $M = 1$. In the $M \neq 1$ cases the rate of change of impedance with position is different ahead of and behind the fluid interface at any given instant because of the different fluid mobilities. As the $M = 3$ flow progresses the rate of change of impedance with position ahead of and behind the water–oil interface increases. In the $M = 0.3$ case the rate of change of impedance with position ahead of the water–oil interface increases as the flow progresses, but in front of the water–oil interface the rate of change of impedance with position decreases. In both the $M = 1$ and $M \neq 1$ cases the change in impedance at the fluid interface is the same because the pore fluid change is the same and the effect of the pore fluid change on the impedance is not pressure dependent.

3.3. Multiphase flow model

Sections 3.1 and 3.2 have only considered cases where a sharp interface separates the flow of water and oil. We now relax this restriction and allow the oil and water to flow together. The ease with which water or oil can move through a porous rock depends on the local water saturation in the pore spaces. Experimental analysis yields fractional flow curves which quantify the saturation dependent mobility of the oil and water. Modifying Darcy's law to include these effects leads to a transport equation for the water and oil phases, in terms of the relative permeabilities of each phase (Dake 1994).

For simplicity the capillary pressure effects are neglected, but a discussion of the possible influences of capillary pressure is given in section 3.6. The fractional flow for each phase is given by

$$U_{\mathrm{w}} = -\frac{m_{\mathrm{w}}}{\phi}\frac{\mathrm{d}P}{\mathrm{d}x}\bigg|_{\mathrm{w}}, \tag{3.13}$$

$$U_{\mathrm{o}} = -\frac{m_{\mathrm{o}}}{\phi}\frac{\mathrm{d}P}{\mathrm{d}x}\bigg|_{\mathrm{o}}, \tag{3.14}$$

and

$$U = U_{\mathrm{w}} + U_{\mathrm{o}}, \tag{3.15}$$

where the mobilities of each phase are

$$m_{\mathrm{w}} = \frac{K K_{\mathrm{rw}}}{\mu_{\mathrm{w}}} \qquad \text{and} \qquad m_{\mathrm{o}} = \frac{K K_{\mathrm{ro}}}{\mu_{\mathrm{o}}}. \tag{3.16}$$

K_{ro} and K_{rw} are the relative permeabilities of each phase. Fractional flow is defined as the volumetric flow of water divided by the total volumetric flow and can be written as

$$f_{\mathrm{w}}(S) = \frac{U_{\mathrm{w}}}{U} = \frac{m_{\mathrm{w}}}{m_{\mathrm{o}} + m_{\mathrm{w}}}. \tag{3.17}$$

The Buckley–Leverett equation describes one-dimensional immiscible displacement in porous media,

$$\phi\frac{\mathrm{d}x_{\mathrm{s}}}{\mathrm{d}t} = U\frac{\mathrm{d}}{\mathrm{d}S}\left(\frac{m_{\mathrm{w}}}{m_{\mathrm{o}} + m_{\mathrm{w}}}\right), \tag{3.18}$$

where $x_{\mathrm{s}}(t)$ denotes the position of a surface of saturation S at time t (Dake 1994).

Fractional flow is measured experimentally as a function of the water saturation, S, and may be approximated by power law models (Corey 1954). As a simple example a synthetic fractional flow curve is constructed by assuming the relative permeabilities of each phase can be approximated by second-order Corey-type functions,

$$K_{\mathrm{rw}} = aS^{*2} \qquad \text{and} \qquad K_{\mathrm{ro}} = b(1 - S^{*})^2, \tag{3.19}$$

where S^{*} is the normalized saturation,

$$S^{*} = \frac{S - S_{\mathrm{wc}}}{1 - S_{\mathrm{wc}} - S_{\mathrm{or}}}. \tag{3.20}$$

Substituting these equations into (3.17) gives

$$f_{\mathrm{w}}(S^{*}) = \frac{S^{*2}}{c\frac{\mu_{\mathrm{w}}}{\mu_{\mathrm{o}}}(1 - S^{*})^2 + S^{*2}}, \tag{3.21}$$

where $c = b/a$. In this expression the $c\frac{\mu_{\mathrm{w}}}{\mu_{\mathrm{o}}}$ term is a single parameter describing the fractional flow relationship of the fluids in a specific reservoir rock. Equation (3.18) implies that the velocity of a small parcel of fluid is the derivative of the fractional flow as a result, for flows where a heavy oil is displaced (small $c\frac{\mu_{\mathrm{w}}}{\mu_{\mathrm{o}}}$), this equation gives a maximum velocity at an intermediate saturation. This leads to the formation of a saturation shock front at

$$S^{*}_{\mathrm{wf}} = \sqrt{\frac{c\frac{\mu_{\mathrm{w}}}{\mu_{\mathrm{o}}}}{1 + c\frac{\mu_{\mathrm{w}}}{\mu_{\mathrm{o}}}}}. \tag{3.22}$$

To determine the impedance profiles resulting from these types of flows the spatial and temporal evolution of saturation and pore pressure are required. Combining (3.21) and (3.18) leads to the relation

$$\phi\frac{\mathrm{d}x_{\mathrm{s}}}{\mathrm{d}t} = U\left(\frac{2c\frac{\mu_{\mathrm{w}}}{\mu_{\mathrm{o}}}S^{*}(1 - S^{*})}{\left(c\frac{\mu_{\mathrm{w}}}{\mu_{\mathrm{o}}}(S^{*} - 1)^2 + S^{*2}\right)^2}\right). \tag{3.23}$$

This gives the saturation distribution of the residual oil tail relative to the location of the shock front, X_{wf}. However, with constant pressure boundary conditions, the shock front does not propagate at a constant rate because the oil and water have different mobilities. To determine how the saturation evolves in time the Darcy velocity U is written as a function of interface position and a numerical integration scheme is used. The pore pressure evolution is determined by combining (3.13), (3.14) and (3.19), and integrating forward with constant pressure boundary conditions to give

$$x_{\mathrm{s}}(t + \Delta t) = x_{\mathrm{s}}(t) + \left(\frac{2c\frac{\mu_{\mathrm{w}}}{\mu_{\mathrm{o}}}S^{*}(1 - S^{*})}{\left(c\frac{\mu_{\mathrm{w}}}{\mu_{\mathrm{o}}}(S^{*} - 1)^2 + S^{*2}\right)^2}\right)U\Delta t, \tag{3.24}$$

which gives the shape of the saturation front as it propagates along the reservoir. The constants ϕ, μ_{w} and K are chosen such that $\frac{\phi\mu_{\mathrm{w}}}{K} = c\frac{\mu_{\mathrm{w}}}{\mu_{\mathrm{o}}}$, so the velocity $U = 1$ when the domain is oil filled. Although there are no analytic solutions, these flows may be solved numerically by combining the size of the shock front (3.22), the rate of propagation (3.24) and the shape of the residual oil zone (3.23).

Figure 3(*c*) shows saturation profiles along the length of the reservoir for three equally divided time steps; the solid lines correspond to $c\frac{\mu_{\mathrm{w}}}{\mu_{\mathrm{o}}} = 0.4$ and the dashed lines correspond to $c\frac{\mu_{\mathrm{w}}}{\mu_{\mathrm{o}}} = 0.1$. A shock front, propagating at an increasing rate,

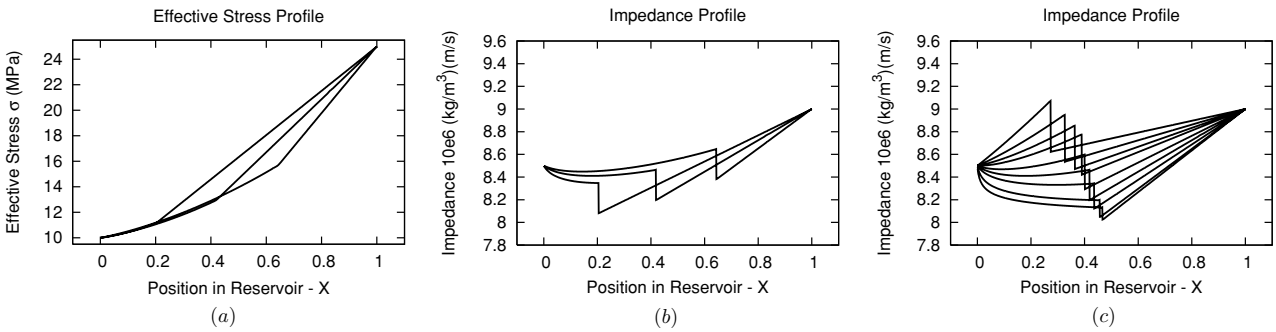

Figure 4. (*a*) Effective stress profiles for a fractional flow. (*b*) Impedance profile for a fractional flow and $M = 3$. (*c*) Impedance profiles for $c\frac{\mu_o}{\mu_w} = 0.05 - 4$.

can be seen and behind it a lengthening residual oil zone. The larger the value of $c\frac{\mu_w}{\mu_o}$ the larger the shock as given by (3.22).

Figure 4(*a*) shows the effective stress profiles for the three equally divided time steps corresponding to a flow where $c\frac{\mu_w}{\mu_o} = 0.4$. The general trend of increasing effective stress towards the production well is the same as in the $M = 1$ and $M = 3$ cases, from sections 3.1 and 3.2. However in figure 4(*a*) the rate of change of effective stress with position is not constant behind the shock front because of the gradual fluid substitution in the residual oil tail. Compared with figure 3(*a*) the change in effective stress for small values of x is small, again due to the residual oil tail.

Impedance profiles of a flow with $c\frac{\mu_w}{\mu_o} = 0.4$ are shown in figure 4(*b*). Again these profiles show some of the same features as the flows from section 3.1 and section 3.2, but with some significant differences. The general trend of increasing impedance towards the production well is observed. However, due to the gradual fluid substitution behind the shock front, the impedance decreases from the injection well to the shock front at early times. In the zone between the injection well and the shock front the steadily increasing effective stress gradually increases the impedance signal, while the decreasing water saturation tends to reduce the impedance. For intermediate times a local minimum can occur in this region.

Figure 4(*c*) shows impedance profiles at $t = 0.4$ for $c\frac{\mu_w}{\mu_o}$ values from 4 to 0.05. As observed earlier, larger $c\frac{\mu_w}{\mu_o}$ values lead to larger impedance jumps at the water–oil interface. In figure 4(*c*) the top curve corresponds to the highest $c\frac{\mu_w}{\mu_o}$ value. The smaller values of $c\frac{\mu_w}{\mu_o}$ correspond to larger fluid mobility contrast; this has an important consequence for the resulting impedance profiles. As the $c\frac{\mu_w}{\mu_o}$ value decreases the effective stress profiles flatten behind the shock front and become steeper in front of the shock front. This effective stress distribution causes the impedance to flatten behind the shock front and become steeper in front of it for smaller values of $c\frac{\mu_w}{\mu_o}$. If the shock front is small this effect could obscure the location of the fluid interface, and complicate the interpretation of the signal.

To summarize the key points from this section, a complex impedance profile results when multiphase effects are included in the flow modelling. Both water saturation and effective stress change gradually and this can result in local minima occurring behind the shock front. The shock front itself may be small and the residual oil tail may then dominate the impedance profile. In these flows impedance is not a simple function of any one physical property; further, a zone in which impedance has not changed but in which both water saturation and effective stress have changed may occur.

3.4. Radial displacement

All the models so far have considered only a linear water flood in the region between the injection and production wells. In this zone the rate of change of effective stress with position is close to linear, leading to simple impedance profiles. Often the near well-bore area, where the rate of change of effective stress with position is not linear, is of interest. For completeness two simple models of radial displacement flow from a water injection well are developed to gain insight into how the impedance of these flows develop in time and space. The first model assumes no contrast in fluid mobility; the second model, in appendix A, accounts for this effect.

3.5. Radial displacement when $M = 1$

Because only the area near the injection well is considered, the pore pressure of the reservoir can be approximated as a pressure source in an unbound incompressible flow domain under steady-state pressure conditions (Dake 1994). The pore pressure at any point in the reservoir is

$$P = -\frac{Q}{2\pi m}\ln\left(\frac{r}{r_0}\right) + P_0, \tag{3.25}$$

for $r_0 < r < 1$, where r is the radius from the centre of the well bore, r_0 is the radius of the well bore, m is the fluid mobility, and P_0 is the injector pressure. There is no contrast in mobility between the oil and water in this model so the pressure field is constant in time. The Darcy velocity of fluid at radius r is given by

$$u = -\nabla P = \frac{Q}{2\pi m r}, \tag{3.26}$$

for $r_0 < r < 1$. A sharp interface is assumed to separate the fluids at all times. Integrating the velocity along the streamlines gives the location of this water front (r_{wf}) as a function of time t,

$$r_{wf} = \sqrt{\frac{tQ}{\pi m}}. \tag{3.27}$$

Figure 5. (*a*) Impedance profiles for a radial flow where $M = 1$.

The water saturation (S) is simply

$$S(r) = \begin{cases} 1 - S_{\text{or}} & r < r_{\text{wf}} \\ Swc & \text{else.} \end{cases} \tag{3.28}$$

Knowing the pore pressure and water saturation distributions allows the impedance to be calculated. Equations (3.28) and (3.8) can be combined with (2.8) to give the impedance at any point in the reservoir.

Figure 5(*a*) shows the impedance of this flow for three equally divided time steps. A sharp increase in impedance occurs near the injector which flattens off away from the injector. A jump in impedance occurs corresponding to the water front. Because of the underlying effective stress distribution, the rate of change of impedance with radius is nonlinear. The shape of the impedance profile, ahead of and behind the water front, is constant in time. The water-front locations show that, although the volumetric flow rate is constant, the front decelerates as it advances. This indicates the signal expected near a water injection well has an initial sharp increase in impedance flattening with distance from the well, and beyond this a jump in impedance propagating outward at a decreasing rate. Near the well bore the impedance change can be dominated by the steep effective stress signal. As the water–oil interface propagates away from the well the effective stress change drops off and the fluid saturation becomes dominant. At early times a complex signal may occur near the well bore if changes in effective stress and water saturation both yield large changes in impedance.

3.6. Frontal instabilities and capillary pressure

In all the models in section 3 the shock front between the water and oil has been assumed to be dynamically stable. However, in general when one fluid displaces another of higher viscosity in a porous medium, frontal instabilities in the form of viscous fingering may occur (Homsey 1987). This results in the development of a water–oil mixing zone in place of the interface and smoothes out any sharp jump in saturation. Further, the presence of a significant capillary pressure between the phases will smooth the saturation profile and the shock front (Dake 1994, Bear 1972).

To explore the effect that a water–oil mixing zone has on the evolution of impedance, a simple model is developed based on the $M \neq 1$ model from section 3.2. A mixing zone centred on the location of the water–oil interface is introduced. The width of the mixing zone grows linearly as the flow progresses, and the fluid mobility in the mixing zone is assumed to be a linear combination of the water and oil mobilities.

The water saturation S is

$$S(x, X_{\text{wf}}) = \begin{cases} S_{\text{wc}} & x < X_{\text{wf}} - \frac{\psi X_{\text{wf}}}{2} \\ 1 - \left(\dfrac{x - \left(X_{\text{wf}} - \frac{\psi X_{\text{wf}}}{2} \right)}{\psi X_{\text{wf}}} \right) & \text{else} \\ 1 - S_{\text{or}} & x > X_{\text{wf}} + \frac{\psi X_{\text{wf}}}{2}, \end{cases} \tag{3.29}$$

where X_{wf} is the centre of the mixing zone and the mixing zone width is $X_{\text{wf}}\psi$. Figure 6(*a*) shows a time series of saturation profiles. The fluid mobility, m, can be written as

$$m(S) = m_{\text{o}} + \left(\frac{S - S_{\text{wc}}}{1 - S_{\text{wc}} - S_{\text{or}}} \right) (m_{\text{w}} - m_{\text{o}}). \tag{3.30}$$

Darcy's law (3.1) can be rearranged to give

$$\frac{\mathrm{d}P}{\mathrm{d}x} = \frac{U\phi}{m(S)}. \tag{3.31}$$

Following the approach of section 3.2 this equation can be integrated and rearranged to give U,

$$U = \frac{\Delta P}{\phi} \left(\int_0^L \frac{1}{m(S)} \, \mathrm{d}x \right)^{-1}, \tag{3.32}$$

where ΔP is the imposed pressure between the wells, which is kept constant, and L is the length of the reservoir. The Darcy velocity, U, changes as the flow progresses because the fluid mobility in the reservoir is changing as fluid is injected and the mixing zone is evolving. The integral in (3.32) can be evaluated by considering the area under the curve of the reciprocal of mobility throughout the reservoir; the details are given in section appendix B. Integrating the reciprocal of the velocity function with respect to X_{wf} gives time, t, as a function of X_{wf}, M and ψ,

$$t(X_{\text{wf}}, M, \psi) = \int_0^{X_{\text{wf}}} \frac{\mathrm{d}X_{\text{wf}}}{U(X_{\text{wf}}, M, \psi)}. \tag{3.33}$$

Solving the resulting expression for the centre of the mixing zone, X_{wf}, gives X_{wf} as a function of time, mobility ratio M, and mixing parameter ψ.

Figure 6(*b*) shows the effective stress along the reservoir for two flows in which $\psi = 0.3$; the solid lines correspond to $M = 3$ and the dashed lines correspond to $M = 0.3$. The resulting effective stress profiles are similar to those from section 3.2, figure 3(*a*), with the key difference being that the effective stress changes smoothly across the oil–water mixing zone.

Figure 6(*c*) shows the impedance profile of three equally divided time steps for a flow in which $\psi = 0.3$; the solid lines correspond to $M = 3$ and the dashed lines correspond to $M = 0.3$. Both cases show an initial increase in impedance away from the injection well followed by decreasing impedance in the water–oil mixing zone and finally an increase in impedance towards the production well. If the width of the mixing zone in this model grows, the change in impedance from one side of the mixing zone to the other decreases, obscuring the fluid movement. Further, as the mixing zone broadens, the

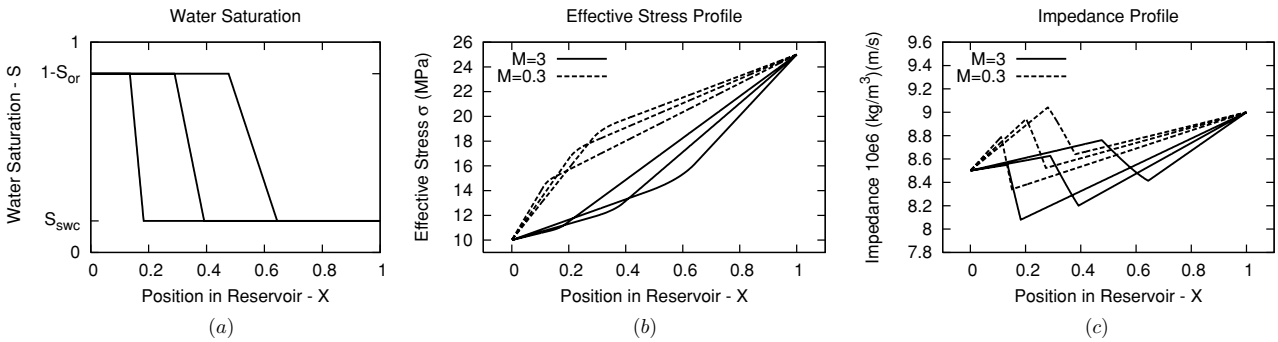

Figure 6. (*a*) Water saturation profiles for $\psi = 0.3$ and $M = 3$. (*b*) Effective stress profiles for mixing flows in which $M = 3$ and $M = 0.3$ when $\psi = 0.3$. (*c*) Impedance profiles for mixing flows in which $M = 3$ and $M = 0.3$ when $\psi = 0.3$.

gradual saturation change may begin to cancel the increase in impedance due to the gradual increase in effective stress. This can result in a flat signal which gives no information about changes in the reservoir.

4. Limitation in time-lapse data analysis

In this section the limitations of using time-lapse data analysis as a reservoir management tool are explored using the modelling of the previous sections. Both qualitative and quantitative analysis methods exist and have different limitations.

4.1. Limitations in qualitative analysis

The simple rock physics and flow modelling of the previous sections have shown that even in a simple case more than one production-related effect can have a leading-order effect on amplitude change as a reservoir is developed.

In the simplest case the water–oil interface is represented as a jump in our synthetic impedance maps and the effective stress changes are manifest as gradual changes in impedance. This simple picture is distorted when the flow model is extended to include more realistic flow behaviours. The introduction of a mobility difference between the fluid phases (section 3.2) results in a shifting effective stress base line and a changing velocity for the water–oil interface. Synthetic impedance maps of the fractional flow model (section 3.3) show a complex signal including local minima behind the water–oil shock front as a result of the development of a residual oil tail. Depending on the parametrization of the relative permeability, a small shock front may occur which is too small to be observed. In such a case only the smooth variations in impedance in the residual oil zone will be observed.

The capillary pressure and fluid mixing model (section 3.6) suggests that the growth of a water–oil mixing zone will result in an expanding zone of smooth impedance change from which interpretation may be difficult. Specifically, if the mixing zone grows to occupy a significant fraction of the reservoir length no fluid interface is observable and the impedance profile may flatten as the effects of water saturation change and effective stress change cancel each other.

Because of these signal complexities, qualitative analysis is limited to identifying areas of impedance change from quiet areas. These data can be used to judge the gross flood efficiency, the location of pressure boundaries and the degree of reservoir compartmentalization. This information is useful in the planning of well sidetracks and new well locations. However, a detailed analysis of flood efficiency and estimations of water breakthrough are not possible because the observed impedance is not a simple function of any one physical property. Further, regions of the reservoir where both water saturation and effective stress have changed but impedance remains the same may occur.

4.2. Limitations in quantitative analysis

Recently, much has been been accomplished in methods for quantitative analysis, which is the estimation of specific reservoir properties such as pressure, saturation, compaction and temperature from time-lapse seismic data. Using multi-component data, amplitude variation with offset models and advanced rock models it is becoming possible to decompose a time-lapse signal into the underlying physical changes. Maps of effective stress, water saturation and temperature derived from these methods can be used as input for reservoir simulations to give estimations of future reservoir performance. This marks a significant advance beyond a qualitative style analysis. However, it is important to recognize that because of the limitations in signal quality, there may be substantial uncertainty associated with reservoir performance estimates. If the total thickness of the reservoir is less than or equal to the resolution of the seismic waves the wave will respond to the average properties over the thickness of the reservoir. If thin high-permeability layers are present in the reservoir, they may accommodate a significant fraction of the volumetric flow rate yet have a sub-seismic size. If the thin high-permeability layers comprise a small fraction of the reservoir thickness, they may be poorly represented in the resulting time-lapse data because their contribution to the total reflection may be below the noise threshold of the data.

A perfect time-lapse inversion method may give the water saturation and effective stress on a discretized grid without error; however uncertainties about sub-discretization length scale fluid movements may remain. Inferences about the fluid

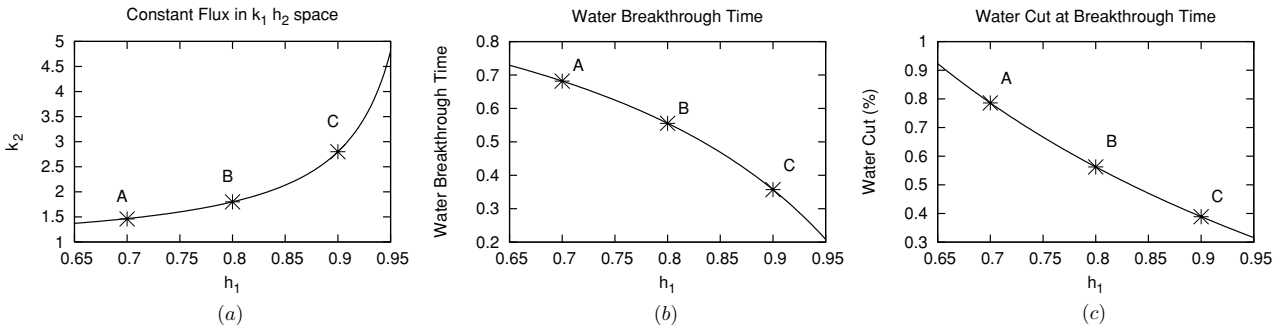

Figure 7. (a) Line of constant flow rate Q in k_1h_2 space. (b) Water breakthrough times as a function of h_1. (c) Water cut at water breakthrough time as a function of h_1.

movement require some knowledge of the spatial distribution of reservoir properties and an associated model of the flow. For example, the flow rate measured at the wells along with estimates of the permeability, porosity and reservoir thickness give an estimate of the water front location after a given time of production, using a model of the flow like those described in section 3. A time-lapse seismic survey may be used to give an independent measure of the location of the water front within the uncertainties described in section 3. If the seismic estimate and the reservoir model estimate do not match it could be due to uncertainty in measurements of the reservoir properties. However, it could also be due to thin high permeability layers, not visible in the time-lapse data, but which transport a significant amount of the fluid. This is an important distinction because it may result in a large uncertainty in predicting water breakthrough times.

To illustrate this point a simple two-layer flow model is introduced in which each layer has a different permeability. Flow in each layer is assumed to be governed by Darcy's law and there is no contrast in mobility between the fluids ($M = 1$) so the pore pressure is the same in each layer and there is no flow between layers. The total thickness of the reservoir horizon is H, h_1 and h_2 are the heights of each layer, and k_1 and k_2 are the permeabilities of each layer.

From well log data it may be known that a dominant layer, h_1, with well characterized permeability, k_1, exists such that $h_1/H > 0.7$. The vertical extent of the reservoir H and k_1 may be estimated from well logs. The measured flow rate Q of this reservoir is the sum of the flow rate in each layer,

$$Q = h_1k_1 + h_2k_2. \tag{4.1}$$

In order to match the measured flow rate in the model the average permeability of the remainder of the reservoir, k_2, is related to h_1, H and Q according to

$$k_2 = \frac{Q - h_1k_1}{H - h_1}. \tag{4.2}$$

Figure 7(a) shows the relationship between k_2 and h_1 which gives a constant flow rate of $Q = 1$ for $k_1 = 0.8$. As an example, the three points A, B and C correspond to three possible values of h_1; 0.7, 0.8 and 0.9 respectively. The water-flood patterns corresponding to cases A–C are shown in figure 8 and the resulting synthetic impedance profiles are shown in figure 9. The interpretation of a time-lapse seismic image of this reservoir (figure 9) may not readily distinguish between these different water-flood patterns. Because of noise and resolution limits on seismic data it is possible that only the large jump in impedance at $X = 0.25$ in figure 9 would be visible and the injected water moving in the thin high permeability layering would be obscured. The possibility of thin high permeability layering has important practical implications.

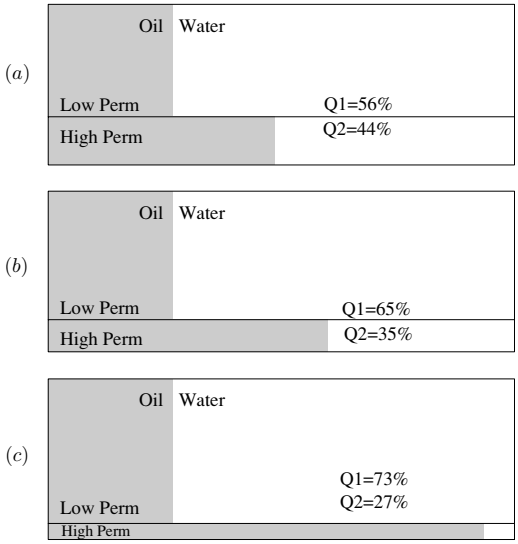

Figure 8. Three possible water-flood patterns that satisfy the observed flow rate and time-lapse seismic signal.

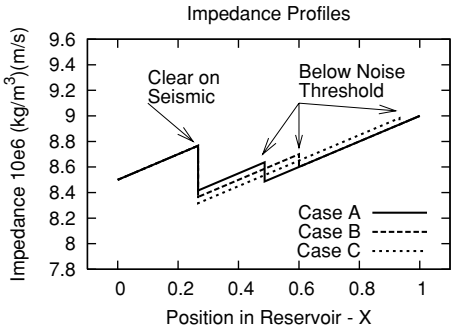

Figure 9. Impedance profiles corresponding to three possible layered reservoirs.

The water breakthrough time and the water cut at breakthrough are different in each of the three cases A, B and C.

Figure 7(*b*) shows the water breakthrough time as a function of h_1. If there is no high permeability layering in the reservoir the water breakthrough will occur at time $T = 0.8$. The addition of a thin high permeability layer in the reservoir results in an earlier water breakthrough time; thinner high permeability layers lead to earlier water breakthrough times. It may be the case that there is no information available to distinguish where on the curve in figure 7(*b*) a reservoir lies. In such a case estimates of water breakthrough time may be off by up to 50%. Figure 7(*c*) shows the water-cut at breakthrough time as a function of h_1. Case A, in which $h_1 = 0.7$, leads to a later water breakthrough time compared to cases B and C but has a larger water cut after the water breakthrough.

The possibility of thin high permeability layers in the reservoir transporting a significant fraction of the injected water may be difficult to constrain by quantitative time-lapse seismic interpretation. This possibility adds considerable uncertainty to estimates of reservoir performance.

5. Conclusions

Acoustic impedance is a function of water saturation and effective stress, both of which change in different ways, both spatially and temporally, as a reservoir is produced. In the absence of pressure barriers, changes in effective stress result in smooth changes in impedance. Water saturation changes result in sharp jumps in impedance or smooth changes depending on the characteristics of the reservoir and the fluids.

These changes will be the largest and easiest to interpret in reservoirs of high porosity and low pressure. It is generally the case that a time-lapse seismic sequence will record the movement of pore fluids and the evolution of the pore pressure but not record the initial transient pressure effects due to individual wells. Near the well bore, changes in effective stress may dominate the impedance change; further from the well changes in water saturation become more dominant.

Qualitative analysis, such as gross judgements of flood efficiency and evaluation of reservoir compartmentalization are possible. This type of analysis is limited by the complexity of the impedance signal resulting when both saturation and effective stress change smoothly, as a result of fractional flow, instabilities or mixing. In such cases the resulting impedance may not be a simple function of either water saturation or effective stress. For example, local minima may develop in a residual oil zone despite the fact that neither effective stress nor water saturation have minima in the area. Further zones of the reservoir which show no change in impedance but where water saturation and effective stress have changed may exist. In flows in which a water–oil mixing zone grows to occupy a significant fraction of the reservoir the resulting impedance profile may flatten as the impedance change due to changes in saturation and pressure interfere.

Quantitative analysis of time-lapse seismic data is becoming possible. This involves using sophisticated rock physics models and advanced seismic techniques to decompose the data into changes in physical properties. The spatial distribution of water saturation and effective stress can be estimated on a discretized grid. This information can be used to make a forward model of reservoir performance. However, the length scales on which significant reservoir fluid movement can occur may be smaller than the length scales of geophysical resolution. For example, the presence of thin high permeability layers in a reservoir may allow a significant fraction of the injected water to propagate faster than the water–oil interface observed in the time-lapse seismic data. Figure 8 shows three possible configurations of a two-layer reservoir under going a water-flood-type production. Each configuration has the same total flow rate. Figure 9 shows the synthetic impedance profiles resulting from each configuration. Because of noise and resolution limitations only the relatively large changes in impedance will be observable in the seismic data. It may be the case that in figure 9 only the large jump in impedance at $X = 0.25$, due to the injected water in the thicker layer, is visible on seismic data and the injected water moving in the thin high permeability layer is not. Figure 7 shows that uncertainty in the reservoir layering can lead to errors of up to 50% in estimates of water breakthrough time. Fluid movement on length scales which are less than the length scales of geophysical resolution leads to large uncertainty in estimates of reservoir performance. The increasing use of sea-floor geophone arrays, and new processing techniques will serve to reduce this uncertainty as resolution increases.

Acknowledgments

The authors would like to acknowledge Ian Jack, Marcus Marsh, Nick White, Iain Gunn and the anonymous reviewers for help in developing this paper.

Appendix A. Radial displacement when $M \neq 1$

Building on the $M = 1$ radial flow model from section 3.5, we now account for a contrast in mobility between the water and oil. To keep the model simple it is assumed that the water–oil interface is stable for all times. The pressure on each side of the interface can be written as

$$P_{\mathrm{w}}(r) = -\frac{Q}{2\pi m_{\mathrm{w}}} \ln\left(\frac{r}{r_0}\right) + P_0 \tag{A.1}$$

$$P_{\mathrm{o}}(r) = -\frac{Q}{2\pi m_{\mathrm{o}}} \ln\left(\frac{r}{r_{\mathrm{inf}}}\right) + P_{\mathrm{I}} \tag{A.2}$$

where P_{w} and P_{o} are the pore pressures behind and in front of the water–oil front, P_0 is the injection well pore pressure and P_{I} is the pressure at the edge of the radius of influence. Combining these two equations with $r = r_{\mathrm{wf}}$ yields an expression for volumetric flow rate as a function of interface position r_{wf},

$$Q = \frac{2M\pi(P_{\mathrm{I}} - P_0)}{M \ln\left(\frac{r_{\mathrm{wf}}}{r_{\mathrm{inf}}}\right) - \ln\left(\frac{r_{\mathrm{wf}}}{r_0}\right)}. \tag{A.3}$$

Substituting this relation into (3.26) gives us the Darcy velocity as a function of radius, r, and interface position, r_{wf}.

$$U = \frac{Q}{r} = \frac{2M\pi(P_1 - P_0)}{M\ln\left(\frac{r_{\mathrm{wf}}}{r_{\mathrm{inf}}}\right) - \ln\left(\frac{r_{\mathrm{wf}}}{r_0}\right)}\frac{1}{r}. \tag{A.4}$$

Integrating the Darcy velocity along the streamlines gives an implicit relation between interface position, r_{wf}, and time, t.

$$t = \int \frac{1}{U}\,\mathrm{d}r = \frac{r^2\left(\ln\left(\frac{r_{\mathrm{wf}}}{r_0}\right) - M\ln\left(\frac{r_{\mathrm{wf}}}{r_i}\right)\right)}{4\pi M(P_0 - P_1)}. \tag{A.5}$$

Appendix B. Velocity calculation

The Darcy velocity of the mixing flows from section 3.6 is calculated from (3.32). The integral quantity in (3.32) can be evaluated by considering the area under the curve of the inverse of mobility along the reservoir, as given by (3.29) and (3.30). These flows go through three stages, in the first stage the leading edge of the mixing zone has not reached the production well, in the second stage the leading edge but not the trailing edge of the mixing zone has reached the production well, and finally the third stage begins as the tailing edge of the mixing zone reaches the production well.

Stage one corresponds to $\left(X_{\mathrm{wf}} + \frac{\psi X_{\mathrm{wf}}}{2}\right) < L$ and the Darcy velocity, U, is

$$U_1(X_{\mathrm{wf}}, M, \psi) = \frac{\Delta P}{\phi} \times \frac{2M(M-1)}{(M-1)((2-\psi)X_{\mathrm{wf}} - M(X_{\mathrm{wf}}(\psi+2)-2)+2M\psi X_{\mathrm{wf}}\ln(M)}, \tag{B.1}$$

where M is the mobility ratio given by (3.3). The mobility of the oil m_{o} is chosen to be one, and ΔP and ϕ are chosen so that $U = 1$ when the reservoir is full of oil. Stage two corresponds to $\left(X_{\mathrm{wf}} + \frac{\psi X_{\mathrm{wf}}}{2}\right) > L$ and $\left(X_{\mathrm{wf}} - \frac{\psi X_{\mathrm{wf}}}{2}\right) < L$; in this case U is

$$U_2(X_{\mathrm{wf}}, M, \psi) = \frac{\Delta P}{\phi} \times \frac{2M(M-1)}{X_{\mathrm{wf}}\left((1-M)(\psi-2)+2M\psi\ln(M) - 2M\psi\ln\left(\frac{2+X_{\mathrm{wf}}(\psi-2)+M(X_{\mathrm{wf}}(\psi+2)-2)}{2\psi X_{\mathrm{wf}}}\right)\right)}. \tag{B.2}$$

Stage three begins when $\left(X_{\mathrm{wf}} - \frac{\psi X_{\mathrm{wf}}}{2}\right) > L$ as the entire mixing zone has left the reservoir; U is

$$U_3(X_{\mathrm{wf}}, M, \psi) = \frac{\Delta P}{\phi}\frac{1}{M}. \tag{B.3}$$

Solving (B.1) for X_{wf} yields

$$X_{\mathrm{wf}}(t, M, \psi) = \frac{2(M - M^2 + \sqrt{M(M-1)^2(t(2-\psi) - M(t(2+\psi)-1)) - 2M\psi t\ln(M)})}{(M-1)(\psi - 2 + M(2+\psi)) - 2M\psi\ln(M)}. \tag{B.4}$$

This expression gives the location of the centre of the water–oil mixing zone as a function of time during stage one. Equation (B.2) cannot be solved for X_{wf} algebraically so a numerical solution is required, and during stage three the Darcy velocity is constant.

References

Bear J 1972 *Dynamics of Fluids in Porous Media* (Minoela, NY: Dover)

Behrens R, Vasco D W and Datta-Gupta A 2004 Seismic imaging of reservoir flow properties: time-lapse amplitude changes *Geophysics* **69** 1425–42

Brevik I 1999 Rock model based inversion of saturation and pressure changes from time lapse seismic data *SEG Expanded Abstracts*

Calvert R 2005 4D technology: where are we, and where are we going? *Geophys. Prospect.* **53** 161–71

Christensen N I and Wang H F 1985 The influence of pore pressure and confining pressure on dynamic elastic properties of Berea sandstone *Geophysics* **50** 207–13

Corey A T 1954 The interrelations between gas and oil relative permeabilities *Producers Mon.* **19** 38

Dake L P 1994 *The Practice of Reservoir Engineering* 1st edn (New York: Elsevier)

Duffaut K, Landro M and Veire H H 2003 Discrimination between pressure and fluid saturation changes from marine multicomponent time-lapse seismic data *Geophysics* **68** 1592–9

Gassmann F 1951 Uber die elastizitat oroser medien (on the elasticity of porous media) *Vierteljahrsshrift der Naturforscenden Gesellschaft in Zurich* **96** 1–23

Gawith D E, Gutteridge P, Watts G F T and Jizba D 1996 Reservoir monitoring of the Magnus field through 4D time-lapse seismic analysis *Pet. Geosci.* **2** 361–72

Gawith D E, Watts G F T and Jizba D 1996 Reservoir monitoring of the Magnus field through 4D time-lapse seismic analysis *Pet. Geosci.* **2** 361–72

Homsey G M 1987 Viscous fingering in porous media *Ann. Rev. Fluid Mech.* **19** 217–311

Jack I 1998 Time-lapse seismic in reservoir management *Society of Exploration Geophysicists Distinguished Instructor Short Course*

Landro M 2001 Discrimination between pressure and fluid saturation changes from time-lapse seismic data *Geophysics* **66** 836–44

Landro M 2002 Uncertainties in quantitative time-lapse seismic analysis *Geophys. Prospect.* **50** 527–38

Nes O M, Holt R M and Fjaer E 2000 The reliability of core data as input to seismic reservoir monitoring studies *Soc. Pet. Eng.* (65180)

Parr R S and Marsh M 2000 Development of 4-D reservoir management West of Shetland *World Oil* **221** 39–47

Raikes S A, Marsh J M and Whitcombe D 2003 BP's increasing systematic use of time-lapse seismic technology *Pet. Geosci.* **9** 7–13

Sherriff R E and Geldart L P 1995 *Exploration Seismology* 1st edn (Cambridge: Cambridge University Press)

Stovas A and Landro M 2005 Fluid-pressure discrimination in anisotropic reservoir rocks—a sensitivity study *Geophysics* **70** 1–11

Stronen L K, Alsos T and Najjar N F 2003 Time-lapse seismic programme at Gullfaks: value and the road ahead *Pet. Geosci.* **9** 35–41

Terzaghi K 1943 *Theoretical Soil Mechanics* 1st edn (New York: Wiley)